PHYSICAL REVIEW D VOLUME 18, NUMBER 9 1 NOVEMBER 1978

Study of the reactions $K_L^0 p \to K_S^0 p$, $\Lambda\pi^+$, $\Sigma^0\pi^+$ and $\Lambda\pi^+\pi^0$ near 550 MeV/c

A. Engler, G. Keyes,* R. W. Kraemer, and M. Tanaka†
Carnegie-Mellon University, Pittsburgh, Pennsylvania 15213

Y. Cho, M. Derrick, D. Lissauer,‡ R. J. Miller,§ J. Schlereth, and R. P. Smith
Argonne National Laboratory, Argonne, Illinois 60439
(Received 19 April 1978)

We present measurements of the differential and polarization cross sections for the reactions $K_L^0 p \to K_S^0 p$, $\Lambda\pi^+$, $\Sigma^0\pi^+$, and $\Lambda\pi^+\pi^0$ made in a hydrogen bubble chamber exposed to a beam of K_L^0 with incident momentum 550 ± 35 MeV/c. The quasielastic data imposes additional constraints on the partial-wave analyses of the KN and $\bar{K}N$ systems. Our data show no strong energy-dependent effects in the region of the reported $\Sigma(1580)$, $J^P = 3/2^-$ state. The phase of the forward regeneration amplitude was found to be about $-160°$ independent of K_L^0 momentum.

I. INTRODUCTION

In this paper we present experimental data on $K_L^0 p$ interactions at 550 ± 35 MeV/c studied in a bubble-chamber exposure. The center-of-mass energy region extends from 1540 to 1610 MeV. Partial cross sections for the reactions $K_L^0 p \to K_S^0 p$, $\pi^+\Lambda, \pi^+\Sigma^0, \pi^+\pi^0\Lambda$, differential cross sections and hyperon polarizations are presented, the three-body final state is analyzed for $Y^*(1385)$ content, the phase of the forward regeneration amplitude is measured, and the energy dependence of the two-body reactions is examined. Experimental details are described including the corrections applied to the data.

The amplitude for the reaction $K_L^0 p \to K_S^0 p$ may be written

$$T = \tfrac{1}{4}(Z_0 + Z_1) - \tfrac{1}{2} Y_1,$$

where Z and Y represent strangeness +1 and −1 amplitudes and the subscripts designate the isospin. Therefore, this reaction allows a study of the interference between the two strangeness amplitudes. One analysis[1] of the $S = +1$ data finds both a resonant and nonresonant solution in the $I = 0$ channel near 1780 MeV. The predictions of the two solutions combined with various Y amplitudes have been compared to our data[2] in a previous publication.

In addition, strong energy-dependent effects in the $S = -1$ system have been observed near 1600 MeV c.m. energy. A narrow peak in the $I = 1$ $K^- d$ total cross section has been seen[3] at 1580 MeV, and one analysis[4] of the reaction $K^- p \to \Lambda\pi^0$ indicates that this peak is due to a $J^P = \frac{3}{2}^-$ state. We have reported[5] partial cross sections and coefficients of the Legendre-polynomial expansion of the differential cross sections and hyperon polarization cross sections. In this paper we give the results based on our final sample.

II. EXPERIMENTAL DETAILS

A. Exposure

The pictures were taken in the Argonne 12-foot hydrogen bubble chamber. Two exposures of 60 000 and 250 000 pictures were made, yielding a total of 310 000 pictures for the experiment. Figure 1 shows the layout used to produce the K_L^0 beam. A heavy metal target was bombarded with the 12-GeV/c proton beam extracted from the Zero Gradient Synchrotron (ZGS) and a dipole bending magnet and horizontal collimator selected negative particles with momentum slightly above 1 GeV/c. This pion beam was steered 135° around the neutrino muon shield and focused on a liquid hydrogen target to produce K^0's by the associated-production reaction $\pi^- p \to \Lambda K^0$. The hydrogen target was cylindrical, 180 cm long and 25 cm in diameter, with its center located 8 m upstream of the beam window of the chamber, which consisted of a 60-cm-horizontal-by-12-cm-vertical opening in lead shielding placed in front of the chamber. Approximately 10^7 pions per pulse gave 2 K_L^0 traversing the chamber per picture. The pion momentum was below the threshold for $\pi^- p \to \Sigma^0 K^0$ so that the K^0 spectrum defined by the window was nearly monoenergetic. Taking into account the energy loss of the pions in the hydrogen target, the forward K^0's produced had a momentum of 550 MeV/c, while the backward ones had 80 MeV/c. The higher-momentum component of the K^0 beam had a momentum spread of 35 MeV/c resulting from the spread in the momentum of the pion beam and the geometrical layout of the experiment. Virtually all of the low-momentum K_L^0's decayed before they entered the chamber. Downstream of the hydrogen target, a bending magnet swept aside charged particles. Approximately 70 cm of lead converted γ's and a final bending magnet swept aside the $e^\pm$ from the converted γ's.

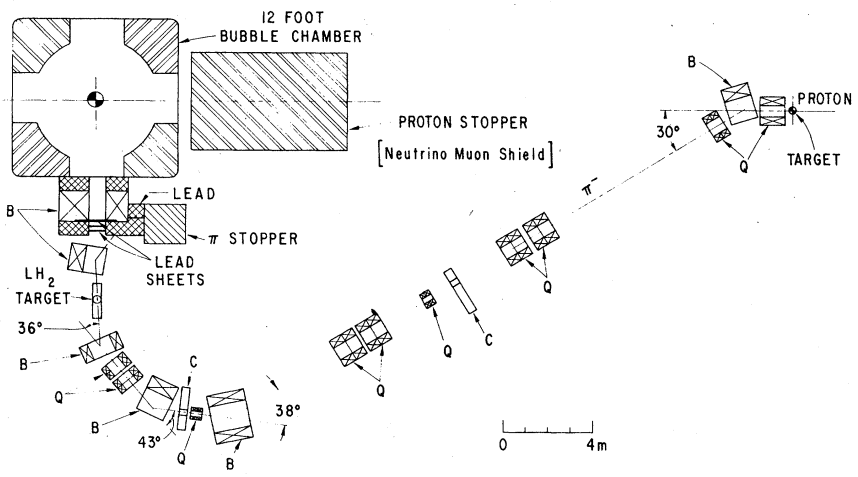

FIG. 1. Layout of the beam-transport system and bubble chamber.

The K^0 beam was selected at 4° to the pion beam to further reduce the background of photons produced from bremsstrahlung of electrons in the beam. Thus γ conversion and Compton scattering in the chamber were not serious background problems. There were approximately 50 one-prong neutron-proton scatters per picture. Although this made scanning more difficult, these events provided no background to the two-prong V^0 topologies of K_S^0 and Λ decay.

The 12-foot bubble chamber is cylindrical in shape and encloses a volume of 26.3 m^3 of which 15.5 m^3 is visible by the four cameras. All four cameras were operated throughout the run although only three views were used to process the data. The chamber magnetic field, produced by a superconducting magnet, was 18 kG.

B. Scanning and measuring

The film was scanned and measured following similar procedures at both institutions. Scanners were instructed to scan all three views for two-prongs (V^0's) since the experiment also included a study of K_L^0 decay.[6] When a V^0 was found, the scanners searched for a recoil lying within a radius of 5 cm of the vertex on all three views and the V^0 was also required to point to that recoil. The length cut (which corresponds to about 20 cm in space) was chosen to eliminate association of random one-prong events with the V^0 vertex. Since the mean decay length for K_S^0 and Λ were 1.8 and 2.8 cm, respectively, this cut produced a minimal bias on the decay-length distributions. The measurements were done at the same time as the scanning on conventional image plane digitizers with a film magnification of 12 ($\frac{1}{4}$ lifesize).

After measurement, the events were processed through a version of the program chain TVGP-SQUAW modified for the 12-foot chamber. Kinematic fits were attempted for the following interaction hypotheses:

$$K_L^0 p \to K_S^0 p \quad , \qquad K_S^0 \to \pi^+\pi^- \tag{1}$$

$$K_L^0 p \to \Lambda\pi^+ \quad , \qquad \Lambda \to p\pi^- \tag{2}$$

$$K_L^0 p \to \Lambda\pi^+\pi^0 \quad , \qquad \Lambda \to p\pi^- \tag{3}$$

and

$$K_L^0 p \to \Sigma^0\pi^+ \quad , \qquad \Sigma^0 \to \Lambda\gamma \ , \ \Lambda \to p\pi^- \tag{4}$$

All of the above reactions are overconstrained if the K_L^0 momentum vector is known. Even though the K_L^0 was unseen, we calculated its space angles by projecting a ray from the interaction vertex in the bubble chamber back to the center of the hydrogen target. The errors were assigned by using the measured profile of the π^- beam and the beam geometry. Reactions (1) and (2) are kinematically overdetermined even if the beam is completely unmeasured. Fits were therefore made with the beam unconstrained to determine the mean K_L^0 momentum and to measure the fraction of scattered K_L^0's in the beam. A pure sample of reaction (1) could be identified by kinematics alone. The purity of the samples of reactions (2)–(4) can be seen in the distribution of the missing mass recoiling from the π^+ shown in Fig. 2. This dis-

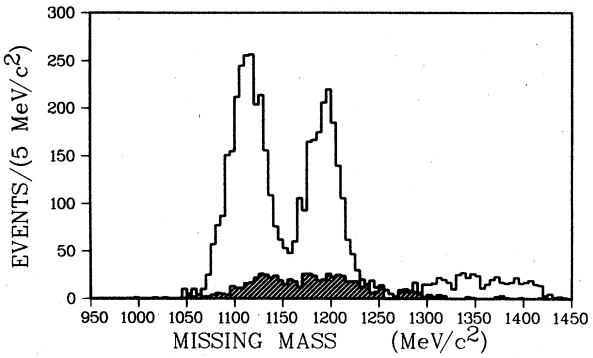

FIG. 2. Missing mass recoiling from the π^+ in events fitting the reactions $K_L^0 p \to \Lambda\pi^+$, $\Sigma^0\pi^+$, and $\pi^+\pi^0\Lambda$. The shaded area represents events giving ambiguous fits.

tribution was calculated from the measured quantities for each event assuming a nominal value of the beam momentum. The ambiguous events, shown as shaded in the histogram, were distributed into the three channels by imposing the following missing-mass (MM) cuts:

$\pi^+\Lambda$ MM$\leq$1155 MeV/c^2,

$\pi^+\Sigma^0$ 1155<MM$\leq$1245 MeV/c^2,

$\pi^+\pi^0\Lambda$ MM>1245 MeV/c^2.

The resulting contamination in each channel is estimated to be less than 3%.

C. Correction for losses

Systematic loss of event topologies with low detection probability or low reconstruction pass rate may introduce biases. The main sources of loss are short tracks and wide V^0 opening angles. Events with short neutral flight paths are likely to be classified by the scanners as three-prong events. Short charged tracks also have low detection probability; this is especially true for short proton recoils. V^0's with wide opening angles may look like one-prong events. Small losses also occur due to interaction or decay of one of the charged tracks close to the vertex.

To determind the cuts needed to eliminate the biases, we have used the Q distributions[7] defined as

$$Q(x)=\int_{x\,\mathrm{min}}^{x} P(x')dx',$$

where $P(x)$ is the probability distribution of the variable x normalized to 1 between the physical limits x_1 and x_2. $Q(x)$ is thus uniformly distributed between 0 and 1 if x_1 and x_2 are the true observable limits on x. By studying the $Q(l)$ distribution, where l is the neutral length for values of $l_{\min}$, the minimum observable neutral length, we find that $l_{\min}\geq 0.5$ cm gives a flat Q distribution for both K_S^0 and Λ decay. The maximum observable neutral length $l_{\max}$ is taken to be the smaller of the distances from the production vertex to the edge of the fiducial volume along the trajectory of the neutral particle, or 20 cm. The latter corresponds to the scanner's template. The weight assigned to each event to compensate for the cuts is

$$\left[\int_{l_{\min}}^{l_{\max}} P(x)dx\right]^{-1}.$$

The lifetimes of the K_S^0 and Λ were measured after after these cuts had been applied to the data using the maximum likelihood method. We found $\tau_{K_S^0}=(0.89\pm0.02)\times10^{-10}$ sec and $\tau_\Lambda=(2.52\pm0.05)\times10^{-10}$ sec in good agreement with the known values. Figure 3 shows the flight-time distributions with the straight lines corresponding to the fitted lifetimes. The $Q(l)$ distributions are shown in Fig. 4(a)–4(d).

For a K_S^0 or Λ of known momentum, the labora-

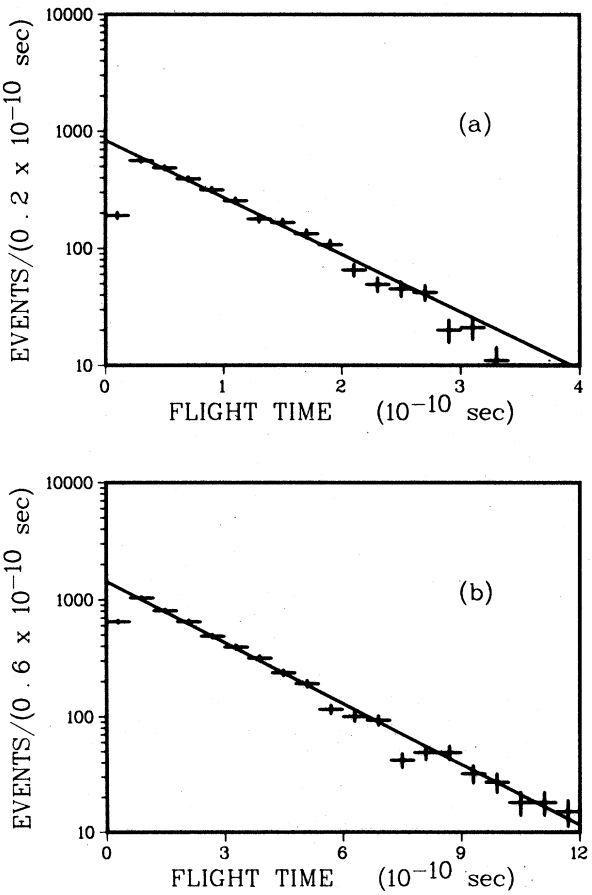

FIG. 3. Flight time distributions for (a) K_S^0 and (b) Λ decays. The lines correspond to the fitted lifetimes given in the text. The events are not corrected for the length cuts.

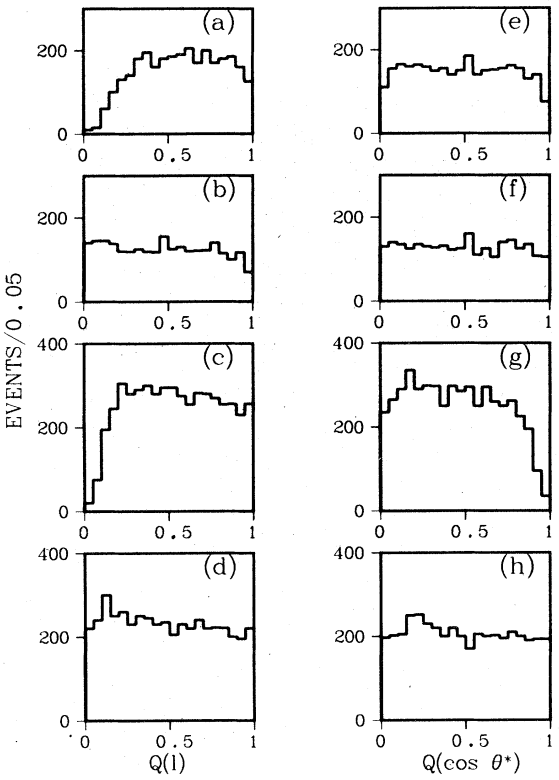

FIG. 4. Q distributions (defined in the text): (a) Q (l) for uncut and (b) cut K_S^0 events and (c) Q (l) for uncut and (d) cut Λ events. (e) The Q ($\cos\theta^*$) distributions for uncut and (f) cut K_S^0 events and (g) for uncut and (h) cut Λ events. The cuts are given in the text.

tory opening angle of the V^0 and the momenta of the decay secondaries depend only on the decay kinematics. We have studied the $Q(\cos\theta^*)$ distributions, where θ^* is the angle between the positive secondary and the neutral particle in its own rest frame for successive cuts on the laboratory momenta of both positive and negative secondaries and for cuts on the laboratory opening angle. We find that the following selections are necessary: for K_S^0 decay, $p_{\pi^+\pi^-}>90$ MeV/c and for Λ decay, $P_p>140$ MeV/c and $P_{\pi^-}>90$ MeV/c. For both decays, events with opening angle $>145°$ were removed. The $Q(\cos\theta^*)$ distributions are shown in Fig. 4(e)–4(h).

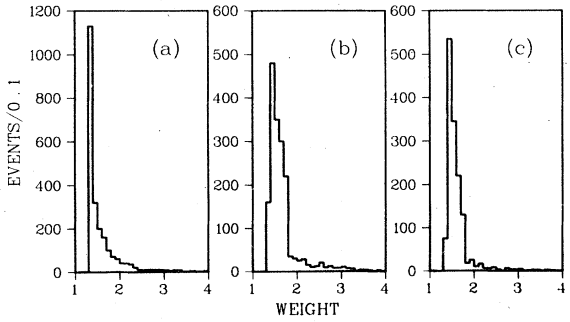

FIG. 5. The distribution of weights used in (a) K_S^0p, (b) $\Lambda\pi^+$, and (c) $\Sigma^0\pi^+$ channels.

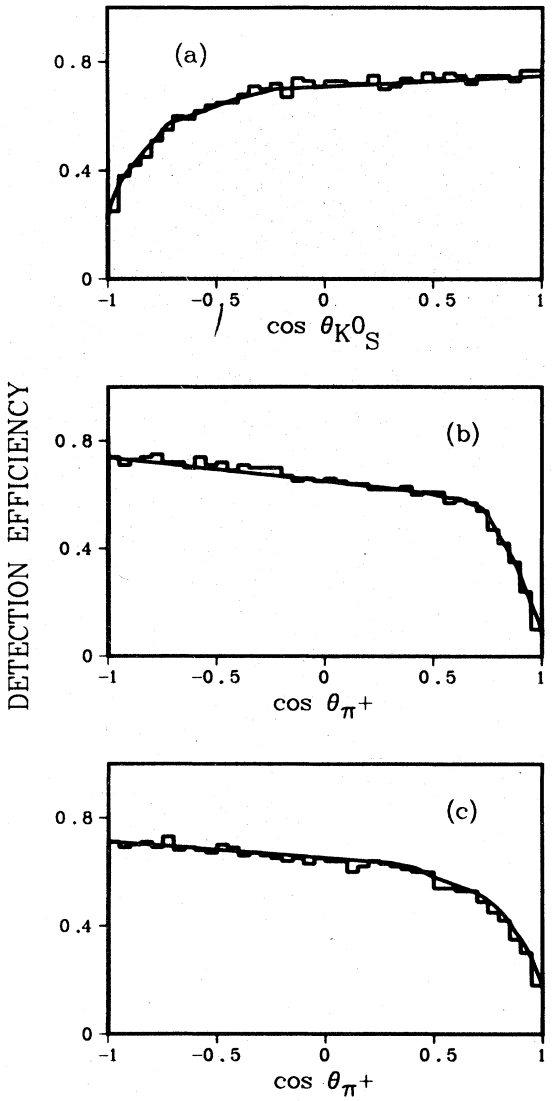

FIG. 6. Detection efficiency as a function of $\cos\theta_{c.m.}$ after the cuts have been made on (a) $K_L^0p\to K_S^0p$, (b) $K_L^0p\to\Lambda\pi^+$, and (c) $K_L^0p\to\Sigma^0\pi^+$ Monte Carlo events. The curves are the average inverse weights calculated as discussed in the text.

The distribution of combined weights is shown in Fig. 5. These analytic weights were checked by generating Monte Carlo events in each channel and applying the same cuts as were applied to the real data. Figure 6 shows the comparison between the distributions of the cut Monte Carlo events as a function of center-of-mass scattering angle with the curves of the detection probability calculated from the analytic weights. Figure 6(a)–6(c) cor-

respond to the three final states $K_S^0 p$, $\Lambda\pi^+$, and $\Sigma^0\pi^+$, respectively. The agreement between the Monte Carlo and the calculated detection probability is good in all cases.

To study the effect of the cuts on the hyperon polarization measurement, five sets of Monte Carlo events were generated in each of the $\pi^+\Lambda$ and $\pi^+\Sigma^0$ channels. In each set a different value of polarization was generated which was taken to be constant across the scattering angular distribution. The Monte Carlo events were then analyzed using the same procedure that was used for the data. The Λ polarization is given by

$$P_\Lambda = (3/\alpha_\Lambda N)\sum_{i=1}^{N} \cos\theta_i w_i , \tag{5}$$

where N is the number of events, α_Λ is the asymmetry parameter, w_i is the weight of the ith event, and θ_i is the angle in the Λ rest frame between the decay proton and the normal to the production plane

$$\hat{n} = (\hat{K}_L^0 \times \hat{\pi}^+)/|\hat{K}_L^0 \times \hat{\pi}^+| . \tag{6}$$

The average Σ^0 polarization is

$$P_\Sigma = -(9/\alpha_\Lambda N)\sum_{i=1}^{N} \cos\beta_i \cos\gamma_i w_i , \tag{7}$$

where β is the angle between the Λ and the normal to the production plane in the Σ^0 rest frame and γ is the angle between the proton and the Λ direction in the Λ rest frame. We observed that the selections systematically shifted the calculated polarization from the input values. The shift was independent of the center-of-mass scattering angle. The calculated polarization after cuts P_c was fitted to a polynomial expansion of the input polarization P_r

$$P_c = \sum_{i=1}^{3} a_i P_r^i . \tag{8}$$

A linear term gave a good fit and we found $P_c(\Lambda) = (1.145\pm0.007) P_r(\Lambda)$ and $P_c(\Sigma^0) = (1.051\pm0.017) P_r(\Sigma^0)$

III. RESULTS

A. Cross sections

1. Normalization method

In order to determine the K_L^0 flux, we have used events assigned to the decay mode $K_L^0 \to \pi^+\pi^-\pi^0$ and used the branching ratio $\Gamma(K_L^0 \to \pi^+\pi^-\pi^0)/\Gamma(K_L^0 \to \text{All})$ found in this experiment.[6] The cross section for channel i is then given by

$$\sigma_i = \frac{N_i}{N_{3\pi}} \frac{M_K}{P_K c\tau n_p} \frac{\epsilon_{3\pi}}{\epsilon_i} \frac{f}{g_i} , \tag{9}$$

where N_i and $N_{3\pi}$ are the number of interactions in channel i and the number of $\pi^+\pi^-\pi^0$ decays within a common fiducial volume, M_K and P_K are the mass and mean momentum of the K_L^0, τ is the K_L^0 mean lifetime, and $n_p = (3.67\pm0.07)\times10^{-5}$ (mb cm)$^{-1}$ is the number of protons per unit volume. The ϵ's are the efficiencies discussed below, f is the branching fraction of K_L^0 into the $\pi^+\pi^-\pi^0$ mode, and g_i is the visible decay fraction of the neutral decaying particle, $g_\Lambda = 0.642\pm0.005$ and $g_{K_S^0} = 0.688\pm0.003$.

2. Efficiencies

Since we have normalized the strong-interaction events that have a 1-prong plus V^0 topology ($N1V$) to $K_L^0 \to \pi^+\pi^-\pi^0$ decays (V^0 topology), we have calculated scanning and measuring efficiencies separately for the two classes of objects. The scanning efficiencies were determined from a double scan of 35% of the film. We found for the $N1V$'s efficiencies of 78% for a single scan and 95% for the double scans, while for V^0's we found efficiencies of 87% and 98%, respectively.

We have also calculated the reconstruction and fitting losses separately for the two topologies. From the $N1V$ events, we rejected those which only gave fits to a scattered K_L^0. We also rejected events which after two measurements only gave one-constraint (1C) or 3C decay fits, but no production fits to reactions (1)–(4). These were decaying neutrals from three-body final states such as $K_S^0 p\pi^0$, $\Sigma^0\pi^+\pi^0$ for the 3C case or three-body K_L^0 decays or decays in which the wrong recoil had been associated with the V^0 for the 1C case. Finally, events which gave no fits to K_S^0 or Λ decay were rejected. In the V^0 topologies, events which gave no three-body decay fits after two measurements were rejected as resulting from scattered K_L^0's. The throughput efficiencies were 96% for V^0's and 87% for $N1V$'s.

We have also made corrections for forward scattering losses. In the center-of-mass interval $0.9 < \cos\theta^* < 1.0$ the detection efficiency after cuts was so low that we deleted this bin from the data and corrected the cross sections by extrapolating to $\cos\theta^* = 1.0$ using the fitted Legendre-polynomial coefficients.

In the reaction $K_L^0 p \to K_S^0 p$, forward scattering corresponds to having a short proton recoil. At an incident K_L^0 momentum of 550 MeV/c, the detection efficiency for the recoil proton may be low even outside of the forward bin, which we have deleted. We have recovered these events by fitting all V candidates to the reaction

$$K_L^0 p \to K_S^0(p) \quad , \qquad K_S^0 \to \pi^+\pi^- \tag{10}$$

where the recoil (p) was unmeasured. About 65%

TABLE I. Summary of cross sections.

Channel	Raw events	Cut events	Weighted events	Events/mb	Correction for $\cos\theta^* > 0.9$	Cross section (mb)
$K_L^0 p \to K_S^0 p$						
Run 1	607	431	713	229		
Run 2	3613	2733	4327	1473		
Total	4220	3164	5040		1.032	3.06 ± 0.34
$K_L^0 p \to \Lambda\pi^+$						
Run 1	371	254	438	213		
Run 2	2481	1823	2997	1362		
Total	2852	2077	3435		1.132	2.47 ± 0.27
$K_L^0 p \to \Sigma^0\pi^+$						
Run 1	364	276	386	213		
Run 2	1931	1485	2405	1362		
Total	2295	1761	2791		1.060	1.88 ± 0.21
$K_L^0 p \to \Lambda\pi^+\pi^0$						
Run 1	64	42	69	213		
Run 2	465	354	568	1362		
Total	529	496	637			0.40 ± 0.05

of the events fitting this reaction were ambiguous with three-body K_L^0 decay. However, we edited a subsample of the events and found no recoils associated with any of the ambiguous events. These ambiguous events were therefore assumed to be K_L^0 decays. A predicted recoil was calculated for the unique events and if the editor found a recoil, the predicted length was compared to the actual length. The distribution of predicted and actual lengths agreed well, although for a few events for which the predicted length was long (>10 cm), the editor found no long recoil. These were probably $K_L^0 p \to K_S^0 p$ events from a scattered K_L^0. The total correction for loss of events with short proton recoils was 5.5% of the $K_S^0 p$ events.

3. Results

The event numbers, corrections and cross sections measured are summarized in Table I. The errors on the cross sections include the statistical error (2.2%), normalization error (4.6%), and the uncertainty on the correction for $\cos\theta^* > 0.9$ (0.5%). We have also included an additional 10% to allow for systematic effects in the normalization. Contributions to the systematic uncertainty include the contamination in two-body channels from three-body reactions $K_L^0 p \to K_S^0 p\pi^0$, $K_S^0 n\pi^+$, $\Sigma^0\pi^+\pi^-$, contamination in the $\Lambda\pi^+$ sample from $\Sigma^0\pi^+$ and vice versa, and the presence of decays of scattered K_L^0's in the $K_L^0 \to \pi^+\pi^-\pi^0$ events.

B. Differential cross sections of the two-body final states

A preliminary analysis of the two-body reactions (1)–(3) averaged over the K_L^0 momentum spectrum has been reported.[2] We present here the results

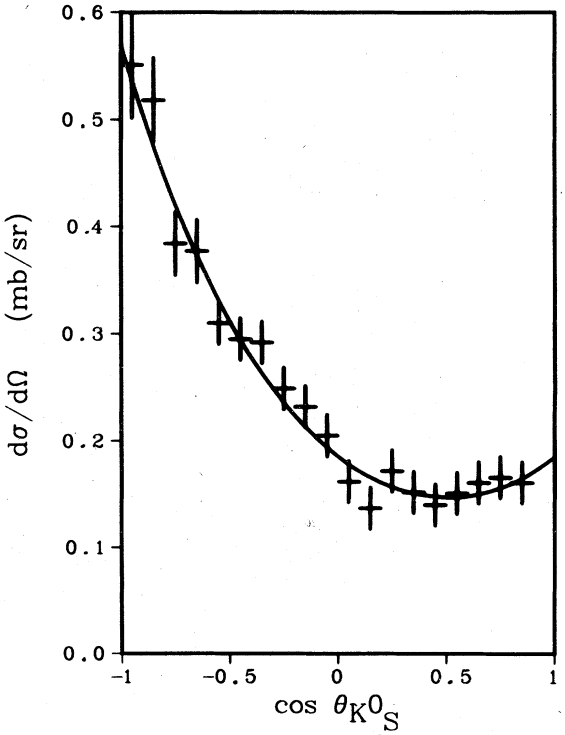

FIG. 7. Differential cross section for $K_L^0 p \to K_S^0 p$ The curve is the result of the second-order fit given in Table II.

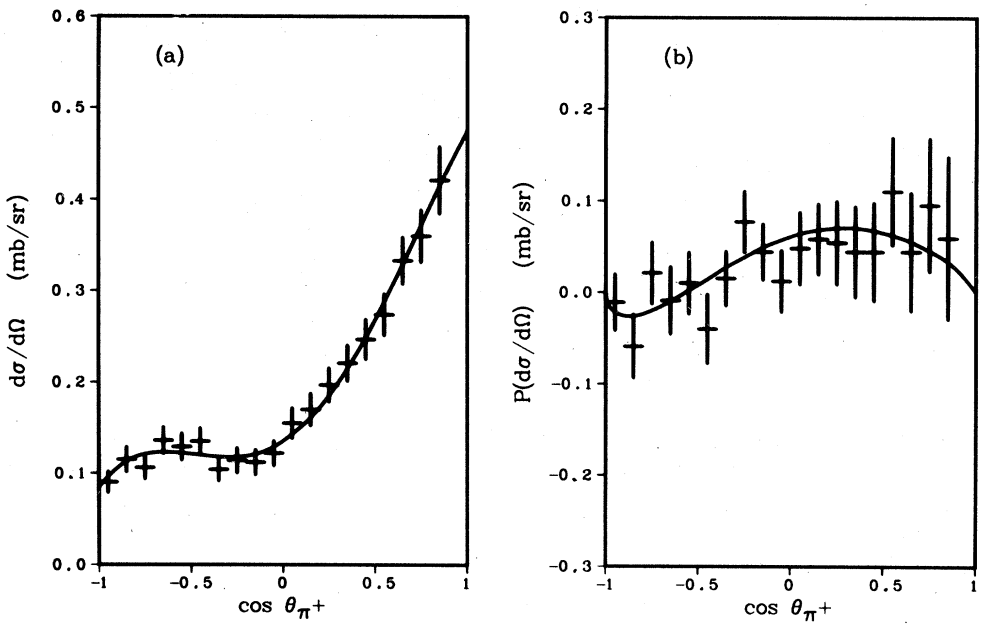

FIG. 8. (a) Different cross section and (b) polarization cross section for $K_L^0 p \to \Lambda\pi^+$. The curves are the result of the fourth-order fit given in Table III.

from the final data sample. The differential and polarization cross sections can be expressed as a sum of polynomials

$$\frac{d\sigma}{d\Omega} = \lambda^2 \sum_{l=0}^{l_{max}} A_l P_l(z) \qquad (11)$$

$$P\left(\frac{d\sigma}{d\Omega}\right) = \lambda^2 \sum_{l=0}^{l_{max}} B_l P_l^1(z), \qquad (12)$$

where P_l and P_l^1 are the Legendre and first associated Legendre polynomials and z is the center-of-mass scattering angle. Equations (11) and (12) were fitted to the data using the maximum-likelihood method in order to extract the coefficients A_l/A_0 and B_l/A_0. The data are shown in Figs. 7–9. For $K_L^0 p \to K_S^0 p$, the polarization of the recoil proton was not measured. The curves drawn on the figures represent the best fit to the data. The data as well as the results of the fits of order 1–4 are listed in Tables II–IV. The $K_S^0 p$ and $\Sigma^0\pi^+$ data were adequately fit by second-order expansions, while the $\Lambda\pi^+$ data required a fourth-order fit.

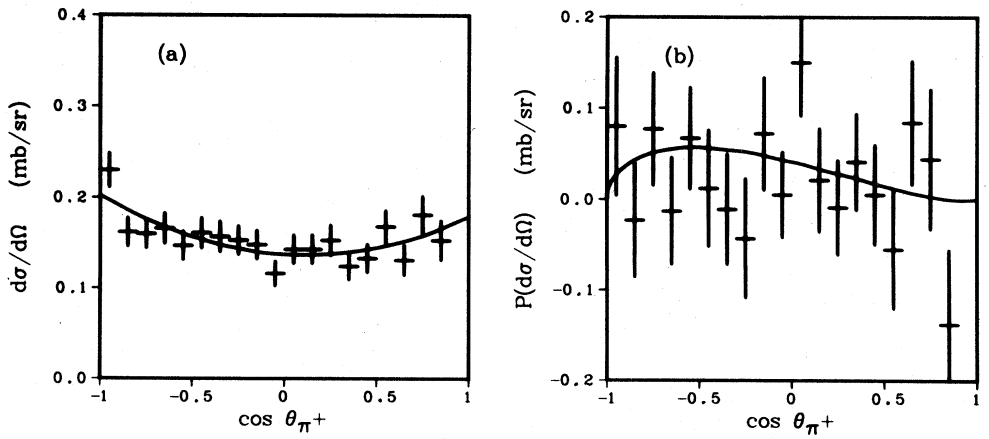

FIG. 9. (a) Differential cross section and (b) polarization cross section for $K_L^0 p \to \Sigma^0\pi^+$. The curves are the result of the second-order fit given in Table IV.

TABLE II. (a) Differential cross section for the reaction $K_L^0 p \to K_S^0 p$. (b) Results of Legendre-polynomial fits.

(a)

$\cos\theta^{*0}_{K^0_S}$	$\frac{d\sigma}{d\Omega}\left(\frac{\text{mb}}{\text{sr}}\right)$
−0.95	0.55 ± 0.05
−0.85	0.52 ± 0.04
−0.75	0.38 ± 0.03
−0.65	0.38 ± 0.03
−0.55	0.31 ± 0.02
−0.45	0.29 ± 0.02
−0.35	0.29 ± 0.02
−0.25	0.25 ± 0.02
−0.15	0.23 ± 0.02
−0.05	0.20 ± 0.02
0.05	0.16 ± 0.02
0.15	0.14 ± 0.02
0.25	0.17 ± 0.02
0.35	0.15 ± 0.02
0.45	0.14 ± 0.02
0.55	0.15 ± 0.02
0.65	0.16 ± 0.02
0.75	0.16 ± 0.02
0.85	0.16 ± 0.02

(b)

	1st order	2nd order	3rd order	4th order
A_1/A_0	−0.67 ± 0.03	−0.71 ± 0.04	−0.73 ± 0.04	−0.72 ± 0.04
A_2/A_0		0.51 ± 0.05	0.51 ± 0.05	0.51 ± 0.05
A_3/A_0			−0.06 ± 0.06	−0.06 ± 0.06
A_4/A_0				0.02 ± 0.07
$P(\chi^2)$	0%	65%	61%	53%

C. Energy dependence of two-body cross sections

We have also calculated the partial cross sections and the A_l/A_0 and B_l/A_0 coefficients as a function of beam energy. In order to measure the energy dependence of the cross sections, the K_L^0 spectrum was determined from a Monte Carlo calculation based on the known π^- beam energy and the beam geometry. This calculated spectrum was compared to the 0C spectrum measured from $K_L^0 \to \pi^+\pi^-\pi^0$ decay and found to have the same mean value and width. The ratio of the fitted momentum spectra of each strong interaction channel to the calculated spectrum was then used to obtain the cross sections as a function of beam energy. The overall normalization was obtained as discussed in Sec. A 3. Our cross-section measurements, which are shown in Fig. 10(a)–10(c), are in agreement with those of other experiments.[8-13]

The results of the fits to the A_l/A_0 and B_l/A_0 coefficients and the individual cross sections can be found in Ref. 5. The differential and polarization cross sections for the three reactions are shown in graphical form in Figs. 11–13.

D. Three-body final state $\Lambda\pi^+\pi^0$

In the reaction $K_L^0 p \to \Lambda\pi^+\pi^0$, $Y_1^*(1385)$ production is possible through a pure isospin-1 channel. The amplitudes for production of $Y_1^{*+}\pi^0$ and $Y_1^{*0}\pi^+$ are equal in magnitude and opposite in sign. Because of background problems and the small event numbers, we have made only a rough measurement of the $Y_1^*\pi$ content of this final state. Using the maximum-likelihood method, we have fit the expression

$$\frac{d\sigma}{dM_{\Lambda\pi^+}{}^2 dM_{\Lambda\pi^0}{}^2} = \alpha_1 + \alpha_2 |T_{\Lambda\pi^0}|^2 + \alpha_3 |T_{\Lambda\pi^+}|^2 \qquad (13)$$

to the Dalitz-plot density, where $\alpha_1+\alpha_2+\alpha_3=1$. We have not included interference terms since the region of overlap of Y_1^* and Y_0^* production

TABLE III. (a) Differential and polarization cross sections for the reaction $K_L^0 p \to \Lambda\pi^+$. (b) Results of Legendre-polynomial fits.

(a)

$\cos\theta^*_{\pi^+}$	$\frac{d\sigma}{d\Omega}\left(\frac{\text{mb}}{\text{sr}}\right)$	$P\left(\frac{d\sigma}{d\Omega}\right)\left(\frac{\text{mb}}{\text{sr}}\right)$
−0.95	0.09±0.01	−0.01±0.03
−0.85	0.11±0.01	−0.05±0.03
−0.75	0.10±0.01	0.02±0.03
−0.65	0.13±0.01	−0.01±0.04
−0.55	0.13±0.01	0.01±0.03
−0.45	0.13±0.02	−0.04±0.04
−0.35	0.10±0.01	0.02±0.03
−0.25	0.11±0.01	0.08±0.03
−0.15	0.11±0.01	0.04±0.03
−0.05	0.12±0.01	0.01±0.03
0.05	0.15±0.02	0.05±0.04
0.15	0.17±0.02	0.06±0.04
0.25	0.20±0.02	0.05±0.05
0.35	0.22±0.02	0.04±0.05
0.45	0.25±0.02	0.04±0.05
0.55	0.27±0.02	0.11±0.06
0.65	0.33±0.03	0.04±0.06
0.75	0.36±0.03	0.09±0.07
0.85	0.42±0.04	−0.06±0.08

(b)

	1st order	2nd order	3rd order	4th order
A_1/A_0	0.65±0.03	0.82±0.04	0.88±0.04	0.85±0.04
A_2/A_0		0.50±0.05	0.59±0.06	0.54±0.07
A_3/A_0			0.22±0.06	0.13±0.08
A_4/A_0				−0.14±0.08
B_1/A_0				
B_2/A_0	0.18±0.08	0.25±0.14	0.23±0.07	0.23±0.07
B_3/A_0		0.14±0.05	0.11±0.06	0.11±0.06
B_4/A_0			−0.05±0.05	−0.05±0.05
				0.00±0.04
$P(\chi^2)$	0%	36%	87%	95%

lies mostly outside of the Dalitz-plot boundary at our beam momentum. Charge symmetry requires α_2 and α_3 to be equal. The resonant amplitude was parametrized as

$$T=\frac{C\sqrt{\Gamma_\beta}}{(E_R-E)-i\Gamma/2}, \quad \Gamma=\Gamma_0\beta_1(q), \tag{14}$$

with E_R and Γ_0 fixed at 1.382 GeV and 0.036 GeV, respectively, Γ_β the partial width for decay of the resonance into $\Lambda\pi$, $\beta_1(q)$ the centrifugal-barrier factor, and C a normalization constant chosen so that $|T|^2=1$ at resonance.

The fit gave $\alpha_2=\alpha_3=0.306\pm0.041$, where α_2 was constrained to equal α_3. Figure 14 shows the $\Lambda\pi^+\pi^0$ Dalitz plot and the solid curves show the phase-space distributions modified by resonant amplitudes. The curves fit the projections with a combined χ^2/DOF of 97.9/54. Thus, we estimate the cross section $\sigma(K_L^0 p \to Y_1^*\pi)$ using the $\Lambda\pi^+\pi^0$ cross section listed in Table I to be 0.28±0.10 mb. The error only includes contributions from the error on $\sigma(K_L^0 p \to \Lambda\pi^+\pi^0)$ and the fitted error on α_2

TABLE IV. (a) Differential and polarization cross section for the reaction $K_L^0 p \to \Sigma^0 \pi^+$. (b) Results of Legendre-polynomial fits.

(a)

$\cos\theta^*_{\pi^+}$	$\frac{d\sigma}{d\Omega}\left(\frac{\text{mb}}{\text{sr}}\right)$	$P\left(\frac{d\sigma}{d\Omega}\right)\left(\frac{\text{mb}}{\text{sr}}\right)$
−0.95	0.23 ± 0.02	0.08 ± 0.08
−0.85	0.16 ± 0.02	−0.02 ± 0.08
−0.75	0.16 ± 0.02	0.08 ± 0.06
−0.65	0.17 ± 0.07	−0.01 ± 0.06
−0.55	0.15 ± 0.02	0.07 ± 0.06
−0.45	0.16 ± 0.02	0.02 ± 0.06
−0.35	0.16 ± 0.02	−0.01 ± 0.06
−0.25	0.15 ± 0.02	−0.04 ± 0.06
−0.15	0.15 ± 0.02	0.07 ± 0.06
−0.05	0.12 ± 0.01	0.00 ± 0.05
0.05	0.14 ± 0.02	0.15 ± 0.06
0.15	0.14 ± 0.02	0.02 ± 0.06
0.25	0.15 ± 0.02	−0.01 ± 0.05
0.35	0.12 ± 0.02	0.04 ± 0.05
0.45	0.13 ± 0.02	0.00 ± 0.06
0.55	0.17 ± 0.02	−0.05 ± 0.07
0.65	0.13 ± 0.02	0.08 ± 0.07
0.75	0.18 ± 0.02	0.04 ± 0.08
0.85	0.15 ± 0.02	−0.14 ± 0.08

(b)

	1st order	2nd order	3rd order	4th order
A_1/A_0	−0.10 ± 0.04	−0.07 ± 0.04	−0.09 ± 0.05	−0.07 ± 0.05
A_2/A_0		0.23 ± 0.06	0.21 ± 0.06	0.23 ± 0.07
A_3/A_0			−0.06 ± 0.08	−0.05 ± 0.08
A_4/A_0				0.06 ± 0.09
B_1/A_0	0.26 ± 0.18	0.26 ± 0.17	0.25 ± 0.16	0.26 ± 0.17
B_2/A_0		−0.08 ± 0.13	−0.08 ± 0.13	−0.10 ± 0.13
B_3/A_0			−0.08 ± 0.11	−0.10 ± 0.11
B_4/A_0				−0.16 ± 0.10
$P(\chi^2)$	13%	46%	35%	23%

and α_3 and does not include systematic effects of contamination by background events. The contribution to background of $\Sigma^0\pi^+\pi^0$ events from resonance production is expected to be small since the branching fraction for decay of Y_1^* into $\Sigma\pi$ is only 0.12. However, the nonresonant $\Sigma^0\pi^+\pi^0$ cross section may be as large as the nonresonant $\Lambda\pi^+\pi^0$ cross section.

E. Phase of the forward regeneration amplitude

The phase of the forward regeneration amplitude was measured using our data and the total-cross-section measurements of K^+n (Ref. 14) and K^-n (Ref. 15),

The phase angle is defined as

$$\tan\phi = \frac{T_I(t=0)}{T_R(t=0)}, \tag{15}$$

where T_R and T_I are the real and imaginary parts of the scattering amplitude. The imaginary part of the amplitude for $K_L^0 p \to K_S^0 p$ is related to the total-cross-section difference

$$T_I(t=0) = \frac{q}{8\pi\hbar c}[\sigma_T(K^+n) - \sigma_T(K^-n)]. \tag{16}$$

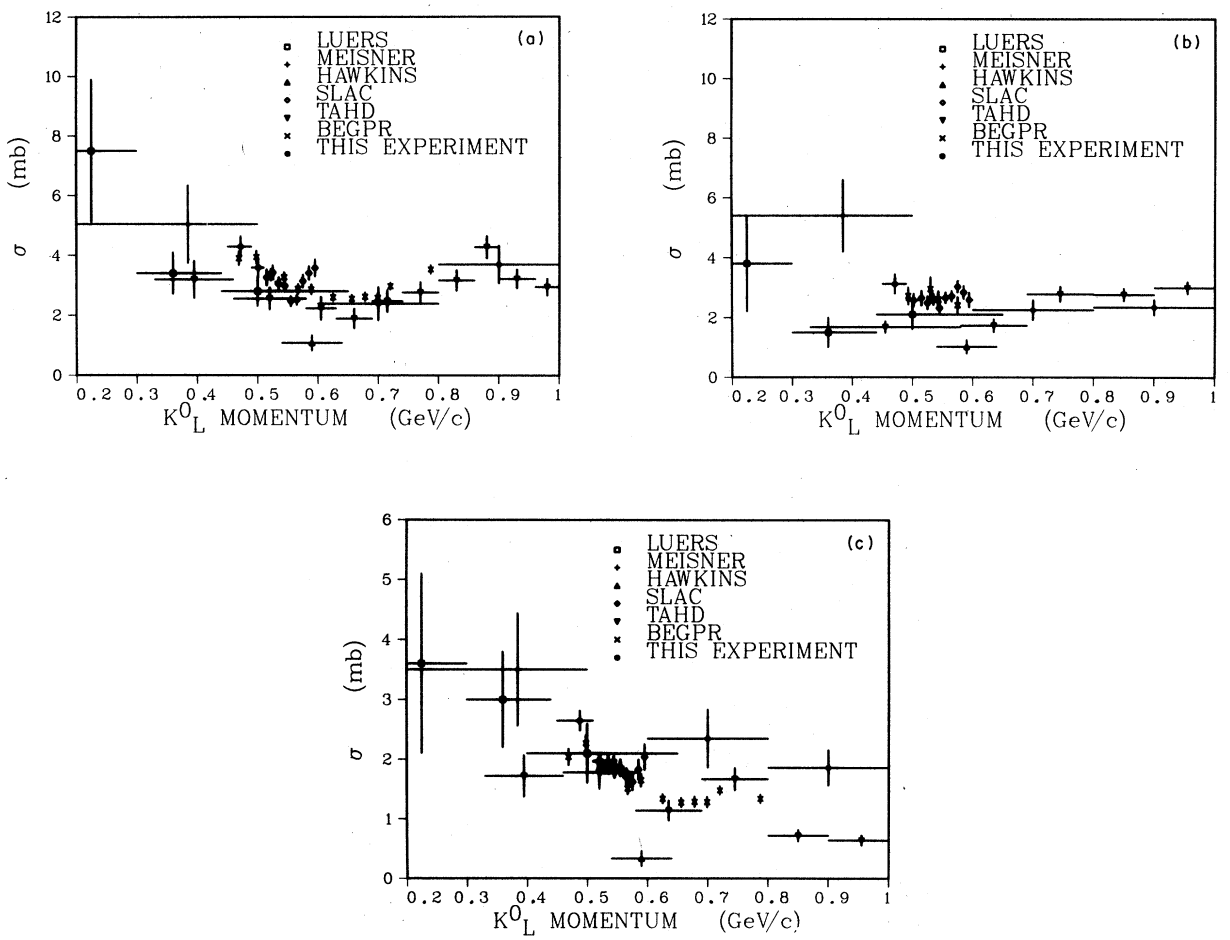

FIG. 10. Cross-section measurements below 1 GeV/c for (a) $K_L^0 p \to K_S^0 p$, (b) $K_L^0 p \to \pi^+\Lambda$, and (c) $K_L^0 p \to \pi^+\Sigma^0$.

Then we define

$$\left.\frac{d\sigma}{dt}\right|_{\text{opt}} = \frac{\pi}{p^2} T_I{}^2(t=0)$$

$$= \frac{\pi}{p^2}\,\frac{q^2}{64(\pi\hbar c)^2}\,(\Delta\sigma_T)^2, \tag{17}$$

where p and q are the center-of-mass momenta of the K_L^0 and $K^\pm$, respectively. The differential cross sections at $t=0$ can be expressed as a sum of Legendre polynomials

$$\left.\frac{d\sigma}{dt}\right|_{t=0} = \frac{\sigma}{4p^2}\sum_{l=0}^{4}(A_l/A_0)P_l(1.0)$$

$$= \frac{\sigma}{4p^2}\sum_{l=0}^{4}(A_l/A_0) \tag{18}$$

since $P_l(1.0)=1.0$. Then, from (15), (17), and (18),

$$\left.\frac{d\sigma}{dt}\right|_{t=0} = \left.\frac{d\sigma}{dt}\right|_{\text{opt}}\left[\frac{1}{\tan^2\phi}+1\right] \tag{19}$$

or

$$\tan\phi = \pm\left[\frac{\left.\frac{d\sigma}{dt}\right|_{t=0}}{\left.\frac{d\sigma}{dt}\right|_{\text{opt}}} - 1\right]^{-1/2}. \tag{20}$$

Dispersion relations and Regge theory require $T_R(t=0)/T_I(t=0)$ to be positive, while $T_I(t=0)$ is found experimentally to be negative from the total-cross-section difference $\Delta\sigma_T$. Thus, ϕ must lie in the third quadrant, and we choose the negative square root.

For this measurement, we have divided out data into five energy bins and used the Legendre expansion determined from a maximum-likelihood fit over the interval $-1.0 \leq \cos\theta^* \leq 0.9$ to give the cross sections at $\cos\theta^*=1$. The results of the fits are given in Table V. Also given in the table are the quantities used to calculate the phase angle. The quantity y is defined as

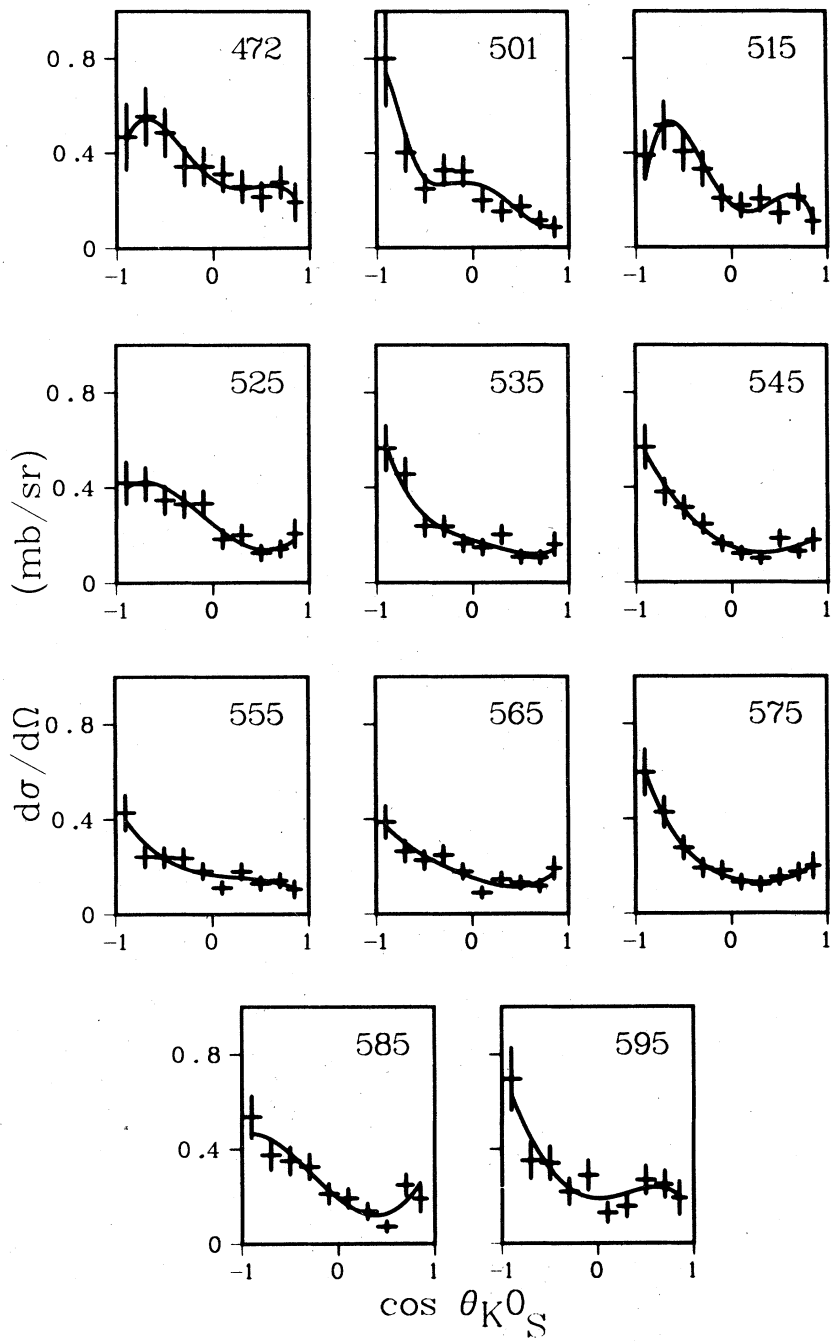

FIG. 11. Differential cross section for $K_L^0 p \to K_S^0 p$ as a function of C.M. energy for the different average K_L^0 lab momenta shown.

$$y = \frac{\left.\frac{d\sigma}{dt}\right|_{t=0}}{\left.\frac{d\sigma}{dt}\right|_{\text{opt}}} - 1. \tag{21}$$

Note that y must be positive in order to obtain physical solutions for ϕ. In other words, the minimum value of $(d\sigma/dt)|_{t=0}$ is the optical point where $T_R = 0$. The corresponding upper bound on the phase angle is $-90°$. The lowest-energy bin in our data gave an unphysical solution, and we found only a lower bound on ϕ given by

$$\phi_L = \tan^{-1}(y + \delta y)^{-1/2}. \tag{22}$$

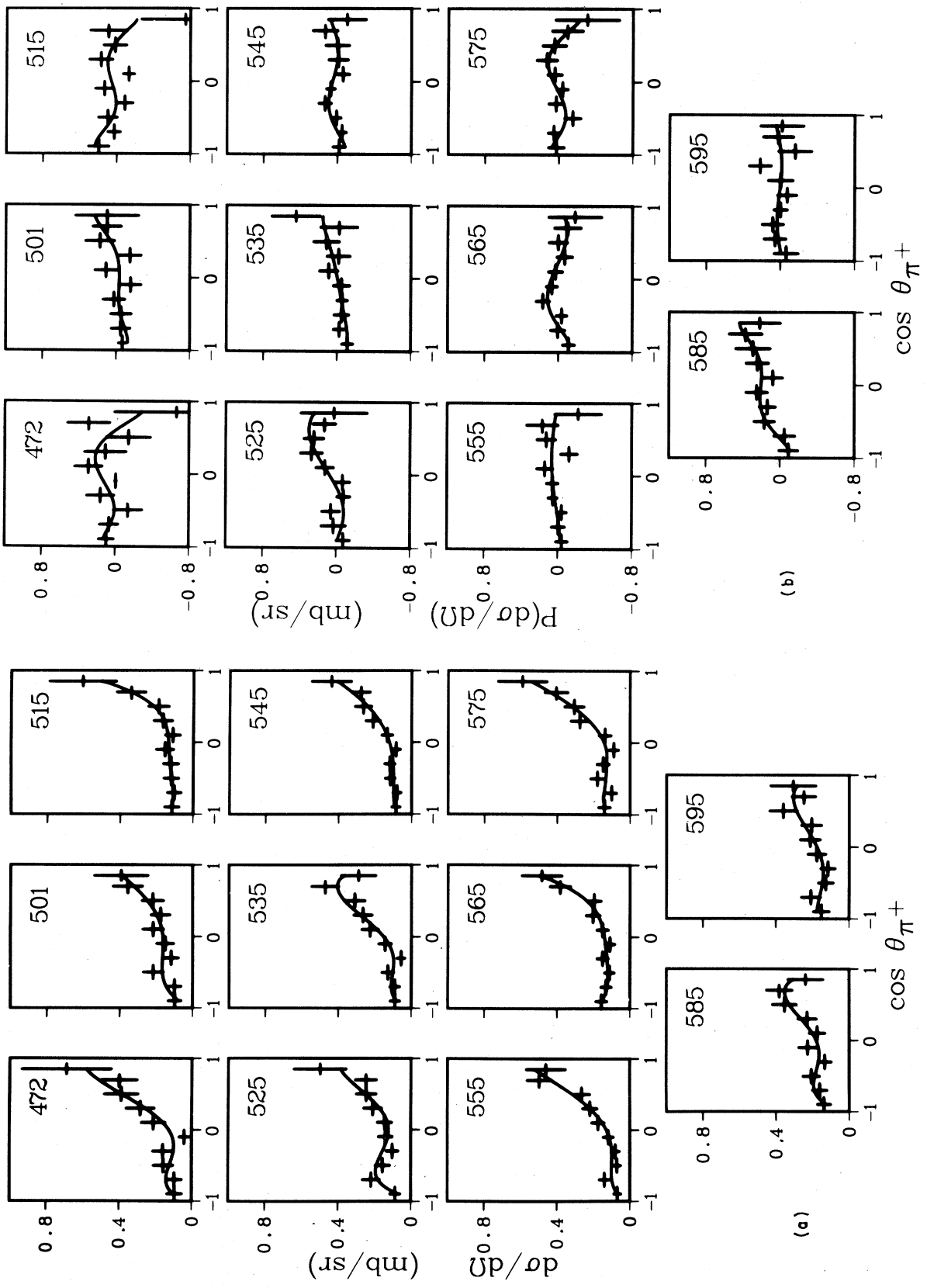

FIG. 12. (a) Differential cross section and (b) polarization cross section for $K_L^0 p \to \pi^+\Lambda$ as a function of C.M. energy for the different average K_L^0 lab momenta.

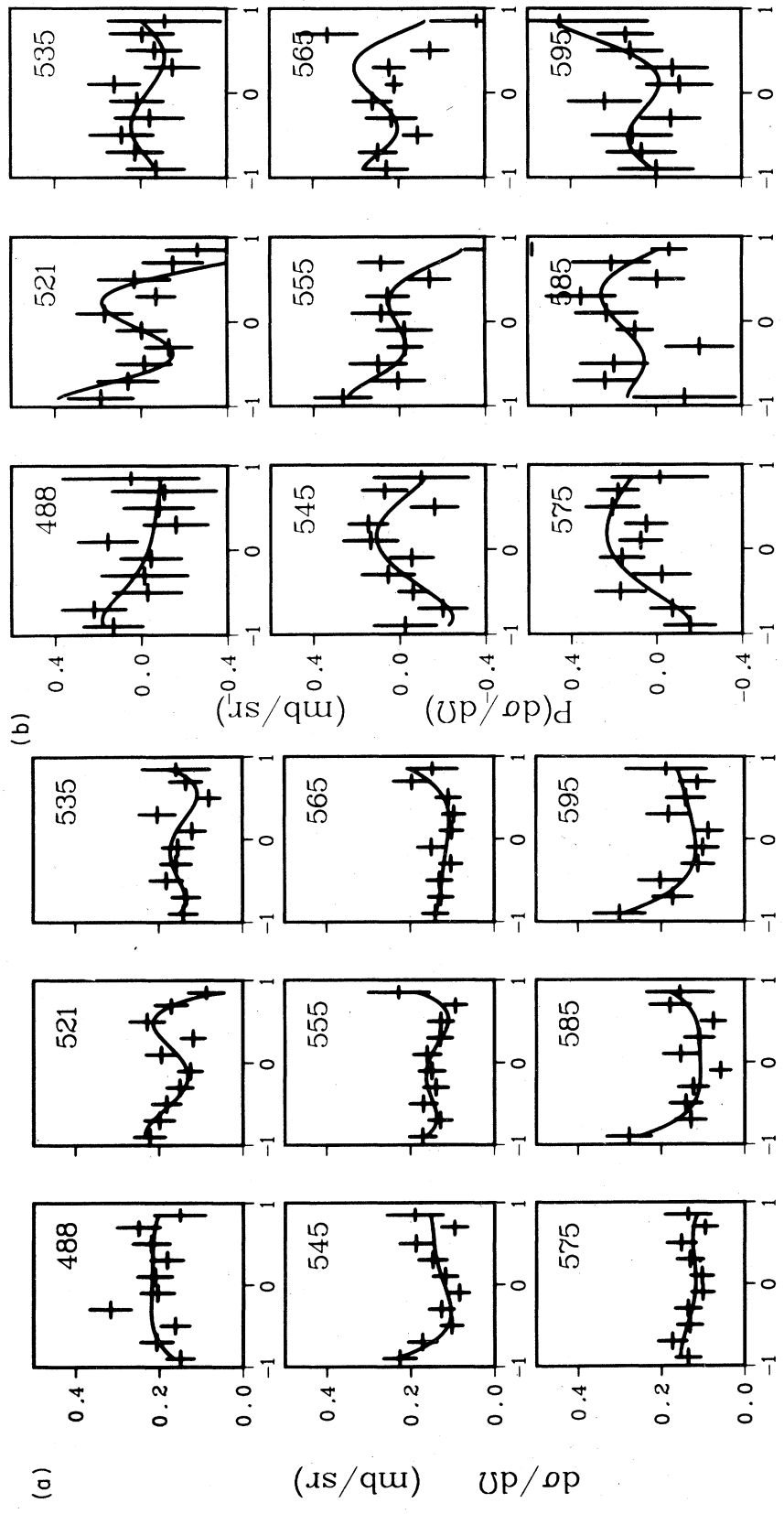

FIG. 13. (a) Differential cross section and (b) polarization cross section for $K_L^0 p \to \pi^+ \Sigma^0$ as a function of c.m. energy for the different average K_L^0 lab momenta.

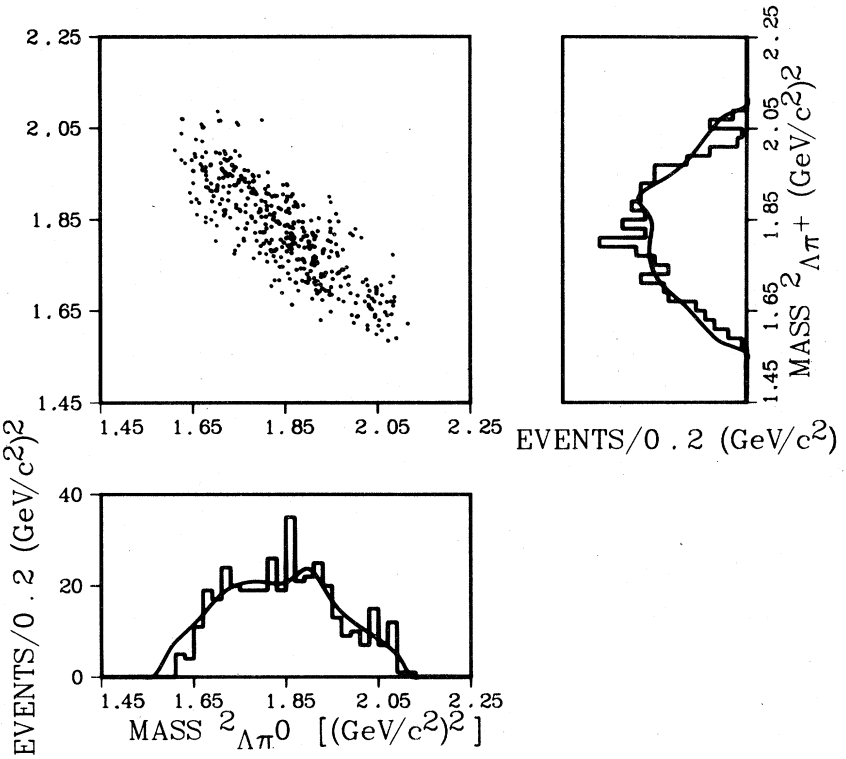

FIG. 14. Dalitz plot for the reaction $K_L^0 p \to \Lambda\pi^+\pi^0$ and the mass-squared projections. The curves are the phase-space predictions modified by resonant amplitudes.

The phase angle is plotted in Fig. 15 along with the results of the Bologna-Edinburgh-Glasgow-Pisa-Rutherford (BEGPR) (Ref. 13) experiment. The results of the two experiments are in agreement.

IV. DISCUSSION

We have compared our preliminary data to predictions of various partial-wave analyses.[2] We will not repeat the detailed comparison here but only make some general remarks. Since the reaction $K_L^0 p \to K_S^0 p$ involves three amplitudes, many combinations are possible. However, in the 1540–1610 MeV mass region, the KN, $I=1$ analyses give very similar results, while the KN, $I=0$ analyses give essentially two different solutions. One of these solutions has a resonant $P_{1/2}$ partial wave around 1780 MeV. The $\bar{K}N$ system has many resonances. The $\bar{K}N$ data have been parametrized in various ways and while the analyses agree on the masses and widths of the most prominent states, they disagree on the existence and properties of less strongly produced ones.

We have compared the predictions of four of the recent analyses of the $\bar{K}N$ system[16-19] combined

TABLE V. Phase of the forward regeneration amplitude.

$\langle P_{K_L^0} \rangle$ (MeV/c)	σ (mb)	$\sum A_I/A_0$	$\left.\frac{d\sigma}{dt}\right\|_{t=0}$ $\left(\frac{\text{mb}}{(\text{GeV}/c)^2}\right)$	$\left.\frac{d\sigma}{dt}\right\|_{\text{opr}}$ $\left(\frac{\text{mb}}{(\text{GeV}/c)^2}\right)$	ϕ
480	4.1±0.3	−0.089±0.38	−1.10±4.7	0.96±0.26	
514	3.9±0.3	0.68 ±0.28	6.1 ±2.6	0.47±0.03	$-164° \pm {}^{5.8}_{2.4}$
537	2.9±0.3	0.73 ±0.22	5.3 ±1.7	0.64±0.07	$-160° \pm {}^{5.0}_{2.9}$
563	2.5±0.3	0.78 ±0.24	4.5 ±1.4	0.77±0.08	$-155° \pm {}^{6.2}_{3.5}$
586	3.2±0.3	0.81 ±0.20	5.7 ±1.5	0.71±0.06	$-159° \pm {}^{3.8}_{2.5}$

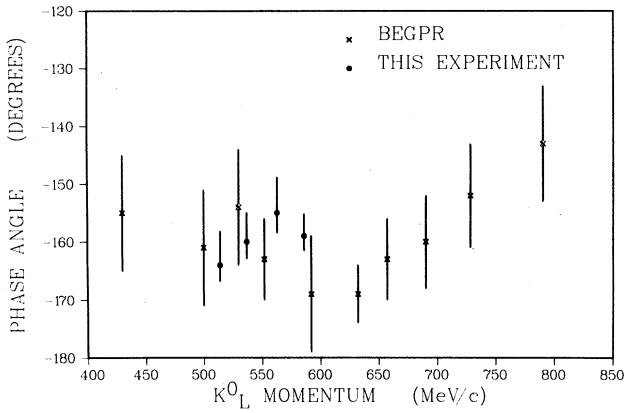

FIG. 15. Phase of the forward regeneration amplitude for low K^0_L momenta.

with three KN amplitudes. These are solutions of BGRT A (Ref. 20) (nonresonant), of BGRT D (resonant), and of Martin.[21] The latter is similar to BGRT D but does not demand a $Z^*(1780)$. The predicted coefficients A_l/A_0 for these different combinations of solutions are presented in Table VI. We note: (a) the BGRT D and Martin $I=0$ amplitudes are very similar and fit the data better than the BGRT A solution. The latter has a positive $S_{1/2}$ wave which interferes destructively with both the KN, $I=1$ $S_{1/2}$ wave which is large and negative, and the $\bar{K}N$ $S_{1/2}$ wave which has a positive real part. This interference gives cross sections which are too low. (b) In the forward direction, our data are flat or only very slightly peaked. Two of the predictions of $\bar{K}N$ analyses[18,19] produce forward peaks by the presence of a positive A_3. This comes from $P_{1/2}$ interfering with the positive tails of the $D_{3/2}(1756)$ and $D_{5/2}(1670)$ resonances. These two solutions require a $P_{1/2}$ resonance around 1640–1670 MeV. Since our data are flat, it suggests either a higher mass or narrower width for this state. (c) None of the predictions fit the data very well since they do not reproduce the large negative A_1 coefficient seen in the data.

The $\Lambda\pi^+$ and $\Sigma^0\pi^+$ states are produced via a pure $I=1$ amplitude in the $\bar{K}N$ system. While data from $K^-p\to\Lambda\pi^0$ is also pure $I=1$, $K^-p\to\Sigma^\pm\pi^+$ involves both $I=0$ and $I=1$ so the $I=1$ part must be unfolded using $K^-p\to\Sigma^0\pi^0$ data. With one exception,[18] all of the $\bar{K}N$ partial-wave analyses have used only K^-p data as input. The A_l/A_0 for the $\Lambda\pi^+_+$ channel are given in Table VII for the various analyses. Since only one isospin channel is involved, there is fair agreement among the predictions in $l\leq 2$ coefficients and in the cross sections. However, the RLIC solution reproduces some features of the data which the others do not. The A_4 coefficient is more negative, in better agreement with the data producing the slight backward dip seen in the differential cross section. The B_2 coefficient, responsible for producing the negative backward dip in the polarization, is more positive resulting from $P_{1/2}$-$P_{3/2}$ interference. The shape coefficients for the $\Sigma^0\pi^+$ channel are given in Table VIII. The A_1 and A_2 are too large in the Martin-UCL prediction. The A_1 results mostly from $S_{1/2}$-$P_{1/2}$ interference, while A_2 results from $S_{1/2}$ interfering with both D waves. In RLIC, B_2 is positive in contrast to the other predictions and to our data. This coefficient results from $S_{1/2}$-$D_{3/2}$ interference.

We concluded in a previous publication[5] that we

TABLE VI. Model predictions of the differential cross section for $K^0_L p\to K^0_S p$. For definitions of amplitudes, see Refs. 16-21.

Amplitudes	σ (mb)	A_1/A_0	A_2/A_0	A_3/A_0	A_4/A_0
Martin-RLIC	4.14	−0.304	0.548	−0.061	−0.004
Martin-LW	3.88	−0.399	0.058	−0.045	−0.002
Martin-CHS	2.77	−0.377	0.538	−0.407	−0.041
Martin-UCL	3.56	0.046	0.403	0.065	−0.246
BGRT D–RLIC	4.18	−0.347	0.432	0.006	−0.020
BGRT D–LW	3.85	−0.406	0.017	−0.015	−0.003
BGRT D–CHS	2.65	−0.455	0.592	−0.319	0.006
BGRT D–UCL	3.51	−0.086	0.356	0.229	−0.248
BGRT A–RLIC	2.70	−0.307	0.325	0.265	0.156
BGRT A–LW	1.94	−0.307	0.173	−0.060	0.043
BGRT A–CHS	1.42	−0.339	0.570	−0.145	0.407
BGRT A–UCL	2.19	−0.588	0.417	0.888	−0.083
This experiment	3.05 ± 0.34	−0.72 ± 0.04	0.51 ± 0.05	−0.06 ± 0.06	0.02 ± 0.07

TABLE VII. Model predictions of (a) the differential cross section and (b) the polarization cross section for $K_L^0 p \to \Lambda\pi^+$. For definitions of amplitudes see Refs. 4 and 17–19.

(a)

Amplitudes	σ (mb)	A_1/A_0	A_2/A_0	A_3/A_0	A_4/A_0
RLIC	2.96	1.046	0.824	0.410	−0.087
LW	2.67	0.995	0.835	0.104	−0.001
Litchfield	3.09	1.026	0.856	0.434	0.038
UCL	2.93	1.023	1.216	0.641	0.216
This experiment	2.47 ± 0.27	0.85 ± 0.04	0.54 ± 0.07	0.13 ± 0.08	−0.14 ± 0.08

(b)

Amplitudes	B_1/A_0	B_2/A_0	B_3/A_0	B_4/A_0
RLIC	0.253	0.097	−0.048	−0.001
LW	0.183	0.050	−0.001	−0.000
Litchfield	0.105	−0.122	−0.193	−0.038
UCL	0.520	0.232	0.079	0.005
This experiment	0.23 ± 0.07	0.11 ± 0.06	−0.05 ± 0.05	0.00 ± 0.04

do not see evidence for a narrow $D_{3/2}$ state at 1580 MeV. Data were presented which showed no structure in the cross sections or coefficients A_1/A_0 and B_1/A_0 in any of the channels $K_S^0 p$, $\Lambda\pi^+$, or $\Sigma^0\pi^+$. Recent results from the BEGPR (Ref. 13) collaboration experiment also confirmed this conclusion. In particular, the A_3 and A_4 coefficients in the $\Lambda\pi^+$ channel, where the resonance effects are supposed to be the strongest, do not go from negative to positive values at the resonant energy. The data presented here show that although there is a dip in the forward direction at one energy, there is no striking change from a forward dip to a forweak peak as the data go

TABLE VIII. Model predictions of (a) the differential cross section and (b) the polarization cross section for $K_L^0 \to \Sigma^0\pi^+$. For definitions of amplitudes, see Ref. 16–19.

(a)

Amplitude	σ (mb)	A_1/A_0	A_2/A_0	A_3/A_0	A_4/A_0
RLIC	1.84	0.047	0.457	0.019	0.007
LW	1.61	−0.055	0.312	−0.119	0.006
CHS	1.73	−0.425	0.479	0.134	0.025
UCL	1.40	−0.484	0.568	−0.019	0.002
This experiment	1.88 ± 0.21	−0.07 ± 0.05	0.23 ± 0.07	−0.05 ± 0.08	0.06 ± 0.09

(b)

Amplitude	B_1/A_0	B_2/A_0	B_3/A_0	B_4/A_0
RLIC	0.529	0.060	0.032	0.009
LW	0.366	0.156	−0.197	0.003
CHS	0.316	−0.198	0.028	0.006
UCL	−0.223	−0.123	−0.107	0.018
This experiment	0.26 ± 0.17	−0.10 ± 0.13	−0.10 ± 0.11	−0.16 ± 0.16

through 1580 MeV. The $K_S^0 p$ and $\Sigma^0\pi^+$ differential cross sections also show no strong energy-dependent effects.

V. CONCLUSIONS

We have measured the differential cross sections and polarization cross sections for the reactions $K_L^0 p \to K_S^0 p$, $\Lambda\pi^+$, and $\Sigma^0\pi^+$ in a hydrogen bubble-chamber experiment in the center-of-mass energy range 1540–1610 MeV. A comparison of our results with the predictions of various partial wave analyses of the KN and $\bar{K}N$ systems shows that the BGRT-D and Martin solutions in the KN, $I=0$ system are in better agreement with the data than the BGRT-A solution. The energy dependence of the same reaction cross sections shows no evidence for a $D_{3/2}$ state at 1580 MeV. In the $\Lambda\pi^+\pi^0$ final state, the cross section $\sigma(K_L^0 p \to \Sigma(1385)\pi)$ was found to be (0.28±0.10 mb). Finally, the phase of the forward regeneration amplitude was measured and found to be constant at about −160° in this energy range.

ACKNOWLEDGMENTS

We would like to thank the technical staff of the ZGS and the 12-foot bubble chamber and the scanning and measuring staffs at both laboratories for their efforts. We would also like to acknowledge the contributions of Gene Fisk, Lloyd Hyman, Brian Musgrave, Don Jankowski, and Jim Russ during the early part of the experiment. This work was supported in part by the U.S. Department of Energy.

---

*Present address: General Electric, Medical Systems Division, Milwaukee, WI 53201.
†Present address: Brookhaven National Laboratory, Upton, NY 11973.
‡Present address: Tel-Aviv University, Tel-Aviv, Israel.
§Present address: Michigan State University, East Lansing, MI 48823.

[1]G. Giacomelli *et al.*, Nucl. Phys. B71, 138 (1974).
[2]Y. Cho *et al.*, Phys. Lett. 60B, 293 (1976).
[3]A. S. Carroll *et al.*, Phys. Rev. Lett. 37, 806 (1976).
[4]P. J. Litchfield, Nucl. Phys. B51, 509 (1974).
[5]A. Engler *et al.*, Phys. Lett. 63B, 231 (1976).
[6]Y. Cho *et al.*, Phys. Rev. D 15, 587 (1977).
[7]R. Y. L. Chu *et al.*, Nucl. Phys. B64, 109 (1973).
[8]D. Luers *et al.*, in *Proceedings of the Aix-en-Provence Conference on Elementary Particles*, (Centre d'Etudes Nucleaires de Saclay, Gif-sur-Yvette, Seine et Oise, Saclay, France, 1961).
[9]C. J. Hawkins, Phys. Rev. 159, 1444 (1967).
[10]G. W. Meisner *et al.*, Phys. Rev. D 4, 2553 (1971).
[11]G. W. Brandenburg *et al.*, Phys. Rev. D 9, 1939 (1974); R. J. Yamartino *et al.*, *ibid.* 10, 9 (1974).
[12]G. Alexander *et al.*, Phys. Lett. 58B, 484 (1975); E. Burkhardt *et al.*, Nucl. Phys. B99, 365 (1975).
[13]L. Bertanza *et al.*, Nucl. Phys. B110, 1 (1976); A Bigi *et al.*, *ibid.* B110, 25 (1976); W. Cameron *et al.*, *ibid.* B132, 189 (1978).
[14]A. S. Carroll *et al.*, Phys. Lett. 45B, 531 (1973).
[15]K. K. Li, private communication. (Update of data from Purdue Conference 1973).
[16]R. Armenteros *et al.*, CERN-Heidelberg-Saclay (CHS) collaboration, Nucl. Phys. B14, 91 (1969).
[17]W. Langbein and F. Wagner (LW), Nucl. Phys. B47, 477 (1972).
[18]G. P. Gopal *et al.*, Rutherford Laboratory–Imperial College (RLIC) collaboration, Nucl. Phys. B119, 362 (1977).
[19]B. R. Martin and M. K. Pidcock, University College London (UCL) Nucl. Phys. B126, 285 (1977).
[20]G. Giacomelli *et al.*, Bologna-Glasgow-Rome-Trieste (BGRT) collaboration, Nucl. Phys. B71, 138 (1974).
[21]B. R. Martin, Nucl. Phys. B94, 413 (1975).